

Power-Rating Balance Control and Reliability Enhancement in Mismatched Photovoltaic Differential Power Processing Systems

Yinxiao Zhu, *Student Member, IEEE*, Huiqing Wen, *Senior Member, IEEE*, Guanying Chu, *Student Member, IEEE*, Xue Wang, *Student Member, IEEE*, Qilin Peng, Yihua Hu, *Senior Member, IEEE*, Lin Jiang, *Member, IEEE*

Abstract—With the increase of the component number, the power stress distribution among differential power processing (DPP) converters, control implementation, system cost, and reliability become the most challenging issues for a practical photovoltaic (PV) DPP system. This paper introduces an improved power rating balance (IPRB) control for the PV-to-Bus based DPP architecture that ensures each PV submodule operate at its true maximum power point (MPP) while achieving more balanced power stress distribution and higher reliability. Specifically, a submodule-level finite-state-machine based MPP tracking (FSM-MPPT) is implemented to guarantee always maximum power yield, while a string-level power rating balancing (PRB) control is adopted to balance the unit-maximum proceeded power by DPP converters based on the built power flow model with respects to the string current. A comprehensive comparison of advanced control strategies for PV-to-Bus DPP architectures, including least power point tracking (LPPT), voltage equalization (VE) based PRB control, and the proposed IPRB, has been carried out with the mission profile-based reliability assessment under different partial shading scenarios. Component-failure-rate based reliability analysis shows that the PV-to-Bus DPP architecture with the proposed IPRB control can significantly improve the system reliability. Main simulation and experimental evaluations are carried out to verify the effectiveness of the proposed control.

Index Terms—Differential power processing, maximum power point tracking, mismatched PV, power rating balancing.

I. INTRODUCTION

GRID parity is the development goal for various renewable energy sources especially for photovoltaic (PV) systems [1]–[5]. As an essential metric in justifying the competitiveness of the PV systems, the levelized cost of energy (LCOE), which is defined by the total capital cost including the operating and maintenance (O&M) over the actual energy output during the lifetime of the PV system, should be lowered in order to ensure the healthy development of PV systems [6]–[10]. Thus, it is essential to ensure high viability of PV with the aim of enhancing the actual energy production while reducing the O&M and replacement costs at the same time [11], [12].

One key issue for PV systems is the mismatching problem, which frequently occurs in a photovoltaic module or submodule level due to partial shading conditions (PSC), hot-spot effect, uneven aging or fabrication and defects [13]. As illustrated in Fig. 1(a), two-third submodules within one PV module are partially shaded, which will result in three peaks in the output characteristics, as demonstrated in Fig. 1(b). Although bypass diodes can be employed to alleviate the negative impact, it still exhibits the effect of multiple peaks, including a global and several possible local maximum power

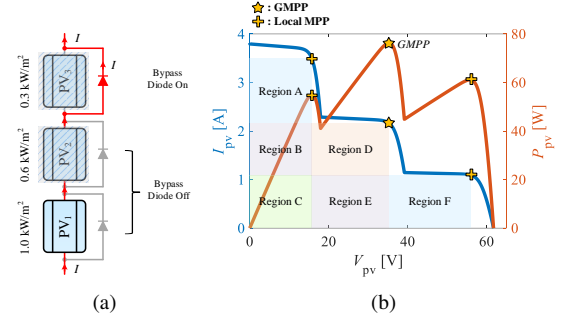


Fig. 1. PV mismatch issue. (a) Current flow with two shaded submodules. (b) Output I - V curve and P - V curve by using bypass diodes.

points (MPPs). Many global maximum power point tracking (GMPP) techniques have been discussed in [14]–[16]. However, they cannot always guarantee the maximum power extraction in each module or submodule under all partial shading conditions. Furthermore, even though the global maximum power point marked with *GMPP* is extracted, the potential power in Region A and F will be lost, as demonstrated in Fig. 1(b). Consequently, the mismatch issue in the PV submodule will result in obvious energy losses and hot-spot phenomena that will go against with the system reliability and lifetime improvement.

Several solutions based on distributed power architecture (DPA) have been developed to eliminate the effect causing by mismatches [21]–[25]. One useful DPA is called DC power optimizer (DCPO), which regulates PV modules operate at their individual MPPs through dedicated power electronics. However, this architecture shows obvious drawback due to high power losses and system cost since all extracted power from PV modules must be processed by their individual converters [26]. Thus, the power rating and reliability of dedicated converters must be set equal to the full power of PV modules, which affects the efficiency and reliability improvement. In order to address this issue, differential power processing (DPP) has been developed and is currently regarded as an effective way of improving the actual power yield under PSCs [27]. By employing the DPP architecture, only a fraction of produced power from PV elements flows through converters, which is beneficial to the power loss reduction. Furthermore, low-voltage-rating power electronics can be utilized in the DPP converters, which shows the benefit of cost-effectiveness. Hence, DPP architectures become a preferred DPA solution for PV mismatching problems.

Recently, different DPP architectures have been introduced, including PV-PV [28]–[35], PV-to-Isolated Port Bus (PV-to-IP) [36]–[39], PV-to-Bus [17]–[20], [40]–[42], and PV-to-

TABLE I
COMPARISON OF CONTROL STRATEGIES FOR PV-TO-BUS DPP ARCHITECTURES

Feature	LPPT [17]	Direct LPPT [18]	Unit-minimum LPPT [19]	VE-based PRB Optimization [20]	This work
Submodule level control	Distributed MPPT	TS-MPPT	Distributed MPPT	Voltage Equalization	FSM-MPPT
Module level control	LPPT	LPPT	PRB	Hybrid	PRB
True MPP operation	Yes	Yes	Yes	No	Yes
Coupling degree	High	Medium	High	Low	Medium
Power distribution	Uneven	Uneven	Even	Even/Uneven	Even
Steady-state oscillation (submodule-/module-level)	Yes/Yes	Yes/No	Yes/Yes	No/No	No/No
Tracking speed (submodule-/module-level)	Slow/Medium	Medium/Fast	Slow/Medium	Fast/Fast	Medium/Fast
Control interface	Yes	No	Yes	No	No

Substring [43]–[45]. Among there DPP architectures, PV-to-Bus DPP shows the advantages of high system efficiency, good galvanic isolation, and easy MPPT implementation for individual PV elements [18]. For instance, all DPP converters in PV-PV architecture are required to participate in the mismatching compensation even though only one or several PV elements are partially shaded. Thus, higher power losses are generated for the PV-PV architecture with the increase in the number of PV elements connected in series among three DPP architectures [38]. For PV-to-IP architecture, true MPP operation for each PV element may become impossible once there is power demanded from the secondary side to PV elements. PV-to-Substring architecture is mainly based on the concept of voltage equalization, which could not provide an exact MPP operation, similar to the PV-to-IP architecture. Meanwhile, considering the unidirectional nature of these configurations, the processed power would be higher than that with bidirectional solutions used in the aforementioned architectures [46]. Thus, this paper will adopt the PV-to-Bus DPP architecture as the preferred architecture in mismatched photovoltaic systems.

For the practical design of photovoltaic PV-to-Bus DPP systems, the most challenging issues include the power stress distribution among DPP converters, control implementation, system cost and reliability considering the development of DPP systems from module level to submodule level in order to address the photovoltaic intra-module mismatch problems. With the number increase of DPP converters, the reliability of DPP converters should be well considered since power devices and capacitors in DPP converters are prone to failure compared with PV elements. It was reported that semiconductor devices such as transistors and diodes attribute 84.81% of the overall failure rate while capacitors attribute 13.81% of the total failure rate [47]–[49]. In order to address this issue, this paper attempts to the system reliability analysis and optimization in the photovoltaic PV-to-Bus DPP architecture by improving the power-rating balance among DPP converters.

In order to address issue, this paper attempts to the system reliability analysis and optimization in the photovoltaic PV-to-Bus DPP architecture by improving the power rating balance among DPP converters. A comparison of main control strategies for PV-to-Bus DPP architectures is summarized in TABLE I.

In [17] and [18], the LPPT control was proposed to minimize the aggregate of total differential power in PV-to-bus architectures. Specifically, [17] firstly introduced perturb and observe (P&O) based LPPT to seek the string current with

total minimum differential power, also as the least power point (LPP), and employed independent MPPT control for each PV modules. Moreover, the individual true MPPT control could be decoupled from the string current regulation since the string current has no effect on the separated MPP operation with a large enough sampling interval. However, it requires n separated MPPT units for n DPP converters, considering the sequential processing structure in micro-controllers. Both the hardware size and implementation cost will be increased, considering the additional auxiliary circuits for multiple micro-controllers [21], [23]. In order to reduce the number of MPPT units, the work in [18] presented the time-sharing MPPT (TS-MPPT) to obtain the true MPP operation with external enable signals. Thus, the total amount of MPPT control units could be reduced to one, which is cost-effective. In the string level, a direct LPPT control was implemented by calculating the optimal string current reference with respect to the least power point, rather than the P&O based seeking algorithm [17]. However, with the string level LPPT, the power distribution in DPP converters are uneven for the majority time. Besides, obvious steady-state oscillations can be observed. To solve this problem, the power rating balancing control was proposed in [19] and [20] intending to seek the power rating balancing point (PRBP) and achieve an even distribution in unit-maximum power. Similar to the study in [17], the work in [19] developed a string level P&O-based control to obtain the even power distribution, namely unit-minimum LPPT (UM-LPPT). Furthermore, the distributed MPPT was employed for approaching individual MPP extraction. To optimize the control effectiveness, the voltage-equalization-based PRB optimization was proposed in [20], which shows a lower control complexity. The voltage equalization (VE) was employed as the submodule control with a suboptimal MPP operation. In the string level optimization, a hybrid control was developed with the LPPT and PRB control, which can improve the system efficiency to a certain extent. Compared with the aforementioned true MPP operation, the VE-based PRB optimization shows the limitation in shifted MPP voltage, which leads to external power losses.

In this paper, an improved power rating balance (IPRB) control for the PV-to-Bus DPP architecture is proposed, ensuring each PV submodules operate at its actual MPPs while achieving a more balanced power stress distribution and higher reliability. Basically, a two-level structure is adopted for the proposed algorithm: submodule-level finite-state-machine based MPP tracking (FSM-MPPT) and string-level power rating balancing (PRB) control. Expressly, FSM-MPPT will al-

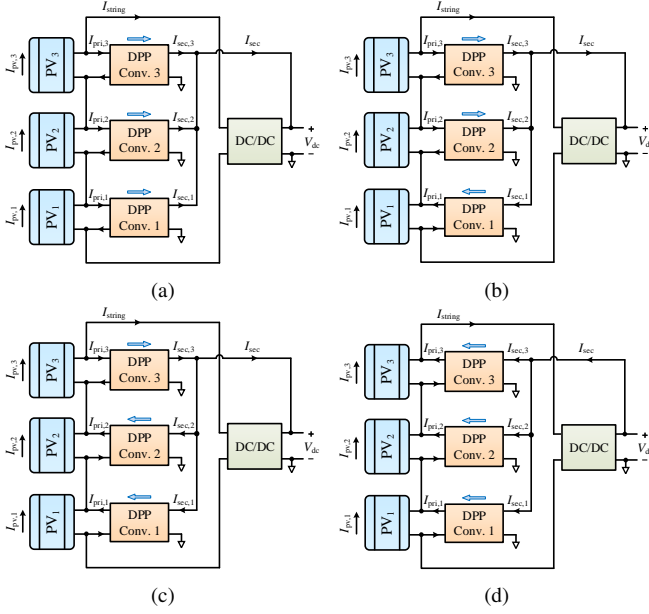


Fig. 2. Operation modes of the PV-bus architecture. (a) *Mode I*. (b) *Mode II*. (c) *Mode III*. (d) *Mode IV*.

ways guarantee maximum power yield. At the same time, PRB control can balance the unit-maximum power proceeded by DPP converters according to the built power flow model with respects to the string current. A comprehensive comparison of advanced control strategies for photovoltaic DPP architectures has been carried out in terms of the total power of DPP converters, the maximum power stress, power losses in power devices, and the reliability under different PSC scenarios. The comparison indicates that the proposed algorithm can achieve a more balanced power stress distribution, which is beneficial for system reliability enhancement. Besides, it can achieve true MPP operation of each submodule with only one control unit, which is cost-effective. Component failure rate based reliability analysis shows that the PV-to-Bus DPP architecture with the proposed IPRB control can significantly improve the system reliability. Main simulations and experimental evaluations are carried out to verify the effectiveness of the proposed control.

II. ANALYSIS OF PV-TO-BUS DPP ARCHITECTURES

A. Power Flow Model for PV-to-Bus DPP Architectures

In the PV-to-bus DPP architecture, the processing power depends on the string current, which directly affects the power flow in each DPP converter. Basically, different operation modes can be classified with respect to the string current. Here, a practical PV module with three submodules is taken as the example for the operation mode analysis.

Assume all three PV submodules operate at their individual MPPs, the PV currents meet the condition “ $I_{pv,1} < I_{pv,2} < I_{pv,3}$ ”, where $I_{pv,1}$, $I_{pv,2}$, $I_{pv,3}$ refers to the MPP current of submodule 1, 2 and 3, respectively. As demonstrated in Fig. 2, four operation modes are classified based on the relationship between submodule currents and the string current I_{string} .

Mode I ($I_{string} \in [0, I_{pv,1}]$): As illustrated in Fig. 2(a), the string current is lower than the minimum value of the PV currents, and all DPP converters extract the power from corresponding submodules.

Mode II ($I_{string} \in (I_{pv,1}, I_{pv,2}]$): In this case, DPP converter 2 and 3 extract power from submodule 2 and 3 while DPP converter 1 will inject power, as demonstrated in Fig. 2(b). Here, I_{string} is set between the submodule current $I_{pv,1}$ and $I_{pv,2}$.

Mode III ($I_{string} \in (I_{pv,2}, I_{pv,3}]$): As shown in Fig. 2(c), in this case, the power of submodule 3 is extracted by DPP converter 3 while other DPP converters will inject current to compensate the current gap between the string and corresponding submodules.

Mode IV ($I_{string} \in (I_{pv,3}, \infty)$): the current distribution of this mode is illustrated in Fig. 2(d). Specifically, all DPP converters will inject current to their corresponding PV submodules.

Based on the classification of operation modes, the power processing by DPP converters can be calculated and developed to a n -submodules generalized model. Neglecting the power loss in DPP converters, the power stress on i^{th} DPP converter could be mathematically expressed as:

$$P_{dpp,i} = V_{pv,i} |I_{string} - I_{pv,i}| \quad (1)$$

Considering the independent MPP operation of PV submodules in the PV-to-Bus DPP architecture, (1) can be rewritten as:

$$P_{dpp,i} = V_{mpp,i} |I_{string} - I_{mpp,i}| \quad (2)$$

Hence, the total processed power in DPP converters, $P_{dpp,tot}$, is expressed by:

$$P_{dpp,tot} = \sum_{i=1}^n P_{dpp,i} = \sum_{i=1}^n V_{mpp,i} |I_{string} - I_{mpp,i}| \quad (3)$$

The unit-maximum processed power in DPP converters, $P_{dpp,max}$, is expressed by:

$$P_{dpp,max} = \max \{P_{dpp,1}, P_{dpp,2}, \dots, P_{dpp,n}\} \quad (4)$$

B. LPP and PRBP Operation

Assume n PV submodules with various MPP current $I_{mpp,i}$ have a similar MPP voltage, namely $V_{mpp,i} \cong V_{mpp}$. The MPP current of the i^{th} PV submodule, $I_{mpp,i}$, is the j^{th} element in ascending order of n MPP currents, which is labeled as $I_{asc,j}$ and $I_{asc,j-1} \leq I_{asc,j}$. In order to minimize the power processed by DPP converters, the least power point tracking control is proposed [17]. The point with total minimum differential power $P_{dpp,tot}$ is named the least power point (LPP). The corresponding string current at LPP, I_{LPP} , can be proved by differentiating the continuous piecewise linear function (3), and expressed as:

$$\begin{cases} I_{LPP} = I_{asc, \frac{n+1}{2}} & , \text{when } n \text{ is odd} \\ I_{LPP} \in [I_{asc, \frac{n}{2}}, I_{asc, \frac{n}{2}+1}] & , \text{when } n \text{ is even} \end{cases} \quad (5)$$

The power stress in DPP converters is also important during the tracking of LPP since unbalanced power distribution may affect the system lifetime and reliability. Although the theoretical rating of each DPP converter should be the same as the maximum output power of PV submodules, many optimizations have been conducted to realize the modular

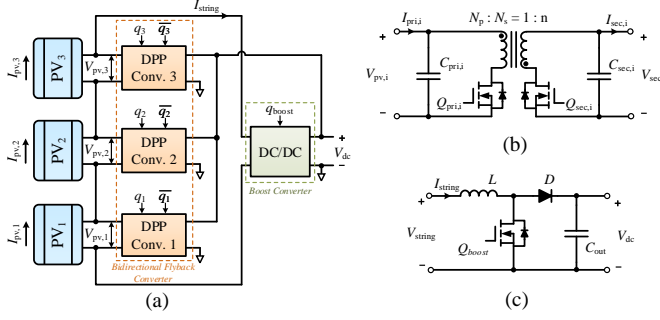


Fig. 3. Configuration of PV-to-bus DPP architecture. (a) Diagram of three-submodule based PV-to-bus DPP architecture. (b) Bidirectional flyback-based DPP converter. (c) Centralized boost converter.

design and reduce the system cost. In [19] and [20], an optimal strategy, namely the power rating balancing (PRB) control, is proposed to seek the unit-minimum differential power and balance the power distribution. Its basic principle is described as the gradient of the power stress in each DPP converter over the string current will change from negative to positive once the string current is larger than the corresponding submodule current. Thus, it is possible to minimize the power distribution in the most stressful DPP converter due to its convex characteristic concerning the string current with (4). Furthermore, the corresponding optimal string current that is named as the power rating balancing point (PRBP) should occur at the middle between $I_{asc,1}$ and $I_{asc,n}$, which is labeled as I_{PRBP} . The maximum power stress in DPP converters with various I_{string} can be expressed by solving (4) as:

$$P_{dpp,max} = \begin{cases} V_{mpp}|I_{string} - I_{asc,n}|, & I_{string} \in [0, I_{PRBP}] \\ V_{mpp}|I_{string} - I_{asc,1}|, & I_{string} \in [I_{PRBP}, \infty) \end{cases} \quad (6)$$

Substitute (5) into (6), then, $P_{dpp,max}$ with I_{string} at LPP could be expressed as:

$$P_{LPP} = \begin{cases} V_{mpp}|I_{LPP} - I_{asc,n}|, & I_{LPP} \in [0, I_{PRBP}] \\ V_{mpp}|I_{LPP} - I_{asc,1}|, & I_{LPP} \in [I_{PRBP}, \infty) \end{cases} \quad (7)$$

At PRBP, the unit-maximum processed power in DPP converters can be expressed by:

$$P_{PRBP} = V_{mpp}|I_{PRBP} - I_{asc,1}| = V_{mpp}|I_{PRBP} - I_{asc,n}| \quad (8)$$

By solving the above equation, the string current corresponding to the PRBP, I_{PRBP} , can be obtained as:

$$I_{PRBP} = \frac{1}{2}(I_{asc,1} + I_{asc,n}) \quad (9)$$

To specify the difference between LPP and PRBP, the impact of operation point on the maximum power stresses of DPP converters under different shading conditions are compared based on the three submodule-based DPP architecture as in Fig. 3. The full irradiance is set as 1.0 kW/m^2 , and no power loss is considered in power converters. The MSX-60 PV module are used in the PV-to-Bus DPP system and their specifications are summarized in TABLE II. Meanwhile, the

TABLE II
SPECIFICATIONS OF MSX-60 PV MODULE

Parameter	Symbol	Value
Number of PV cells	n_s	36
MPP power	P_{mpp}	60W
MPP current	I_{mpp}	3.55A
MPP voltage	V_{mpp}	17.1V
Short-circuit current	I_{sc}	3.8A
Open-circuit voltage	V_{oc}	21.1V
Shunt resistance	R_{sh}	1000Ω
Series resistance	R_s	0.008Ω
Temperature coefficient of I_{sc}	$\alpha_{I_{sc}}$	0.065%/°C
Temperature coefficient of V_{oc}	$\beta_{V_{oc}}$	-0.38%/°C

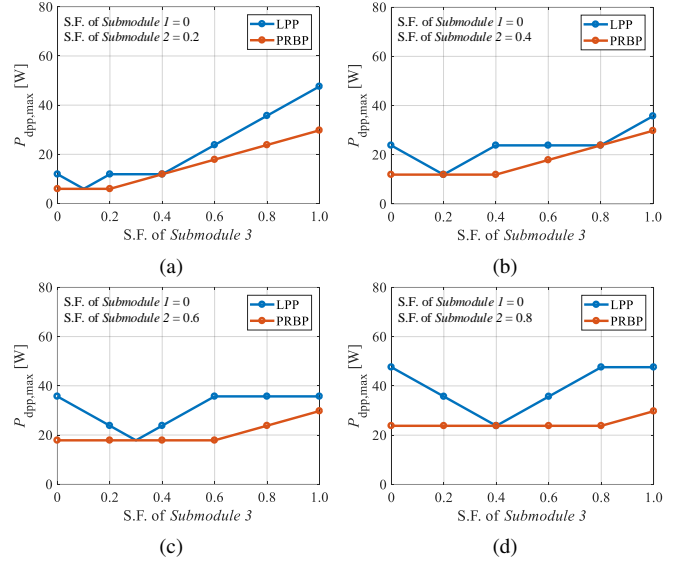


Fig. 4. $P_{dpp,max}$ with respect to the shading factor of submodule 3. (a) S.F.₂ = 0.2. (b) S.F.₂ = 0.4. (c) S.F.₂ = 0.6. (d) S.F.₂ = 0.8.

shading factor (S.F.) is introduced to quantize the shaded level in PV submodules, 'S.F. = 0' and 'S.F. = 1' refers to unshaded and fully shaded, respectively. The S.F. parameters for three submodules are set as: S.F. for submodule 1 is zero, S.F. for submodule 2 will be set as 0.2, 0.4, 0.6 and 0.8, while S.F. of submodule 3 is changing from 0 to 1. As demonstrated in Fig. 4, the maximum power stress $P_{dpp,max}$ with PRBP operation will be no larger than that with LPP under any shading condition, which indicates the effectiveness of the PRBP in reducing the power stress in DPP converters.

III. PROPOSED IPRB CONTROL

In previous works, the seeking for PRBP could be approached with perturb and observe (P&O) based UM-LPPT in [19] or VE-based PRB optimization in [20]. However, these works do not balance the trade-off among the control interface, steady-state oscillations, and true MPP power extraction. Besides, the effect of non-ideal characteristics in power electronics is ignored by these works.

To addressed these issues, an improved power rating balancing (IPRB) control is proposed to balance the uneven differential power in this paper. The proposed IPRB control is divided into two sections, including finite-state machine-based MPPT (FSM-MPPT) control for DPP converters and power rating balancing control for string current regulation. The system configuration is demonstrated in Fig. 3. Considering the requirement in isolation and bidirectional power transmission capability, the bidirectional flyback converter (BFC), as

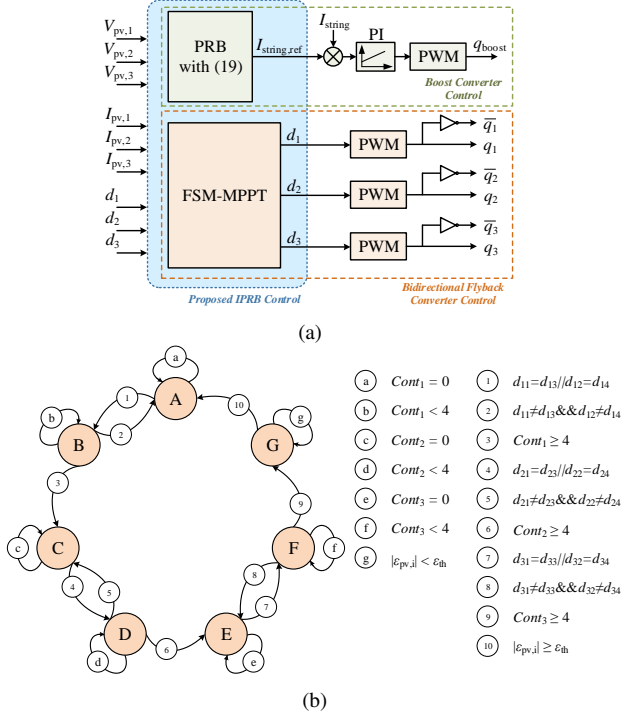


Fig. 5. System control. (a) Control diagram. (b) State transition diagram (STD) of FSM-MPPT control.

Fig. 3(b), is employed as the DPP converter in this paper. The outputs of BFCs are directly connected with system output, as drawn in Fig. 3(a). By using this configuration, differential power is only processed one time comparing with connecting to the input of the centralized converter. Additionally, the direct connection reduces implementation complexity and enhances system reliability due to decouple processed power in the centralized converter. Developed to AC applications, the centralized DC/DC converter contributes a probability to regulate DC-link voltage. Submodule power extraction is obtained by BFCs through differential power injection and removal. As illustrated in Fig. 3(c), the boost converter is employed as the centralized converter to regulate string current for approaching PRB control. The system control diagram is illustrated in Fig. 5.

A. Submodule-BFC-level FSM-MPPT Control

In PV-to-bus architecture, every submodule equips an MPPT controller for maximum power extraction as a conventional solution. However, the independent MPPT controller enhances the implementation cost and hardware size with the increase in auxiliary power supplies and circuits [21], [23]. Hence, the finite state machine (FSM) technique is utilized to provide the sequential processing capability for each PV submodules and reduce the number of MPPT controllers in this paper.

As illustrated in Fig. 5(a), the proposed FSM-MPPT control would deliver the corresponding duty cycle for each BFCs based on the sampled submodule currents and voltages. The state transition diagram (STD), as in Fig. 5(b), is introduced to detail the tracking procedure of proposed FSM-MPPT control, and the state specifications is summarized in TABLE III. Notably, d_i represents duty cycle for i DPP converter. d_{i1} , d_{i2} , d_{i3} , d_{i4} refer to the duty in last four perturbation intervals, respectively. The $Cont_i$ represents the counter for the duty

TABLE III
SPECIFICATIONS OF STATE TRANSITION DIAGRAM

State	Flag	d_1	d_2	d_3	$Cont_1$	$Cont_2$	$Cont_3$
A	1	P	F	F	0	0	0
B		P	F	F	$Cont_1++$	0	0
C	0	F	P	F	$Cont_1$	0	0
D		F	P	F	$Cont_1$	$Cont_2++$	0
E	-1	F	F	P	$Cont_1$	$Cont_2$	0
F		F	F	P	$Cont_1$	$Cont_2$	$Cont_3++$
G		F	F	F	$Cont_1$	$Cont_2$	$Cont_3$

*P = Perturbed; F = Fixed

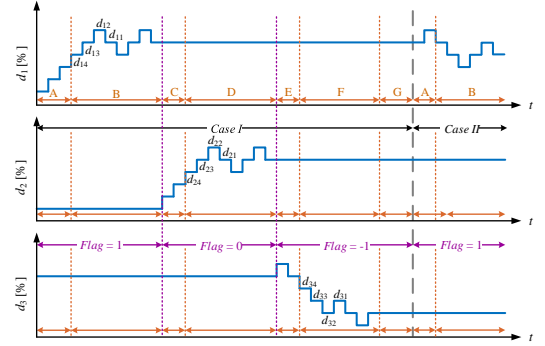


Fig. 6. Example duty cycle regulation with FSM-MPPT control.

cycle of i^{th} BFC and used to detect the stability of achieved submodule MPP. The value of $Flag$ refers to the tracking of MPP in the relative submodule.

An example tracking procedure for a three submodule-based PV-to-Bus DPP architecture with proposed FSM-MPPT is illustrated in Fig. 6. Initially, the submodule MPPT sequence would begin at State A for submodule 1 with the $Flag$ set at 1. In this state, only the d_1 for controlling the corresponding BFC for PV submodule 1 would perturb, and the counters are continuously equal to zero. The perturbation of d_1 is based on the output power variation of submodule 1 between two sampling intervals. For example, the sampled voltage and current of PV submodule 1 are $V_{pv,1}(t-1)$ and $I_{pv,1}(t-1)$ at the previous, and $V_{pv,1}(t)$ and $I_{pv,1}(t)$ at present sampling intervals, respectively. If $P_{pv,1}(t) > P_{pv,1}(t-1)$ but $V_{pv,1}(t) < V_{pv,1}(t-1)$ or $P_{pv,1}(t) < P_{pv,1}(t-1)$ but $V_{pv,1}(t) > V_{pv,1}(t-1)$, the value of duty cycle d_1 for DPP converter 1 would increase for moving the PV operation point to close to the MPP. Otherwise, the value of d_1 would decrease. State A would be continued until the sign occurred, which is as $d_{11} = d_{13}$ or $d_{12} = d_{14}$ in ① of Fig. 5(b). This condition symbolizes that the steady-state three-level perturbation is achieved in the MPPT for submodule 1, and the state would transit to State B. In State B, the counter $Cont_1$ is used to record the continuous repeat frequency of $d_{11} = d_{13}$ or $d_{12} = d_{14}$, or $Cont_1$ would return to 0 if the sign repeat is discontinuous. Notably, the d_1 would continue its perturbation in this state as that in State A. If $Cont_1 \geq 4$, as obtained ③ in Fig. 5(b), d_1 would be fixed, the operation of proposed FSM-MPPT would transit to State C, and $Flag$ would switch to '0' for tracking the MPP of submodule 2. In State C, only d_2 would perturb and follow the concept above for perturbing d_1 in State A, but d_1 and d_3 are fixed here. Until three-level perturbation of d_2 is matched, as $d_{21} = d_{23}$ or $d_{22} = d_{24}$,

State C would transit to State D and $Cont_2$ begins to count as $Cont_1$ in State B. In State D, $Cont_2$ would record the repeat time of three-level perturbation, and d_2 would continue the perturbation until $Cont_2 \geq 4$. Then, d_2 would be fixed, the operation state would transit to State E, and $Flag$ would switch to '-1', and the proposed FSM-MPPT would track the MPP of submodule 3. Similarly, d_3 would perturb and $Cont_3 = 0$ in State E till the sign of three-level perturbation occurred. As $d_{31} = d_{33}$ or $d_{32} = d_{34}$ occurred, State E transit to State F, d_3 continues the perturbation, and $Cont_3$ begins to add up. The state of FSM-MPPT would transit to State G until $Cont_3 \geq 4$ is obtained. In State G, the value of $Flag$, d_i and $Cont_i$ would be fixed till the irradiance changed. Once the irradiance change is detected, as Case I transit to Case II in Fig. 6, the operation state of proposed FSM-MPPT would transit to State A, $Flag$ would be refreshed as 1, and begin to track submodules MPPs sequentially. The subsequent tracking procedure is repeated as aforementioned. Notably, the steady-state oscillations in each PV submodules by implementing the proposed FSM-MPPT.

In the practical operation, the irradiance is easily changed, which affects the mismatches of PV submodules and the operation state of the proposed control. Hence, a reliable criterion for detecting the irradiance change is a crucial issue for control design. To address this issue, the output power variation of the i PV submodule between two adjacent sampling intervals $\varepsilon_{pv,i}$ is introduced in the proposed FSM-MPPT control. Meanwhile, a preset threshold ε_{th} is used to validate the environmental dynamics and eliminate perturbation-induced steady-state power variation. Basically, the irradiance change is detected by $\varepsilon_{pv,i}$ is larger than the absolute value of ε_{th} , and the mathematical qualification could be delivered by

$$\varepsilon_{pv,i} = \left| \frac{P_{pv,i}(t) - P_{pv,i}(t-1)}{P_{pv,i}(t-1)} \right| \geq \varepsilon_{th} \quad (10)$$

where $P_{pv,i}(t)$ and $P_{pv,i}(t-1)$ represent the output power of submodule i in the present and previous sampling intervals. The threshold ε_{th} is set to 0.05. Once $\varepsilon_{pv,i}$ is larger than ε_{th} , as obtained (10), the irradiance condition would be considered as changed, and the MPPs are required to be renewed. Here, the operation state in proposed FSM-MPPT would be switched to State A, and $Flag$ would be renewed and set at 1. Then, the proposed control would follow the tracking sequence to approach the MPPs of all submodules.

B. String-Current-level Power Rating Balancing Control

Balanced processing power in BFCs is approached by implementing the proposed PRB control, as illustrated in Fig. 5(a). Generally, PRB control can balance the unit-maximum power through BFCs by regulating string current I_{string} . For I_{string} regulation, a PI controller is employed to control the centralized boost converter. Meanwhile, the calculation of reference for string current $I_{string,ref}$ is a key issue. Based on the analysis above, an ideal $I_{string,ref}$ for balancing processing power could be selected at the corresponding value of PRBP and expressed as

$$I_{string,ref} = I_{PRBP} = \frac{I_{pv,max} + I_{pv,min}}{2} \quad (11)$$

where $I_{pv,max}$ and $I_{pv,min}$ are maximum and minimum value of submodule PV current and expressed as

$$\begin{cases} I_{pv,max} = \max \{I_{pv,1}, I_{pv,2}, I_{pv,3}\} \\ I_{pv,min} = \min \{I_{pv,1}, I_{pv,2}, I_{pv,3}\} \end{cases} \quad (12)$$

However, the power injection from string introduces the power losses in actual operation. Hence, the ideal explained of $I_{string,ref}$ in (11) is not suitable for the non-ideal operation. In non-ideal operations, the balancing power P_{PRBP} is rewritten as

$$\begin{aligned} P_{PRBP} &\cong V_{pv,min} |I_{PRBP} - I_{pv,min}| + P_{loss} \\ &\cong V_{pv,max} |I_{PRBP} - I_{pv,max}| \end{aligned} \quad (13)$$

where $V_{pv,min}$ and $V_{pv,max}$ represent the correlated voltage of submodules with $I_{pv,min}$ and $I_{pv,max}$ and expressed as

$$\begin{cases} V_{pv,max} = \arg \max_{V_{pv,max} \in \{V_{pv,1}, V_{pv,2}, V_{pv,3}\}} \{I_{pv,1}, I_{pv,2}, I_{pv,3}\} \\ V_{pv,min} = \arg \min_{V_{pv,max} \in \{V_{pv,1}, V_{pv,2}, V_{pv,3}\}} \{I_{pv,1}, I_{pv,2}, I_{pv,3}\} \end{cases} \quad (14)$$

The power loss in DPP converter is represented by P_{loss} , which expressed as

$$P_{loss} = P_{sw} + P_{mg} \quad (15)$$

To simplify the approach, the frequency-related loss in magnetic components P_{mg} is ignored. The power loss in MOSFETs, P_{sw} , can be expressed as:

$$\begin{aligned} P_{sw} &\cong R_{DS,on} i_{sw,RMS}^2 + t_{tr} V_{sw} i_{sw,peak} f_{sw} \\ &\quad + (V_{GS}^2 C_{iss} + V_{sw}^2 C_{oss}) f_{sw} \end{aligned} \quad (16)$$

where $R_{DS,on}$, $i_{sw,RMS}$ and $i_{sw,peak}$ refer to static drain-to-source on-resistance, RMS current and peak current through the MOSFET, respectively. V_{sw} and V_{GS} represent the voltage across the MOSFET and the gate driving voltage. f_{sw} , C_{iss} , C_{oss} represent the switching frequency, input and output capacitance of MOSFETs, respectively.

Then, rewrite (13) with (15),

$$AI_{PRBP}^2 + BI_{PRBP} + C = 0 \quad (17)$$

Here,

$$\begin{aligned} A &= R_{DS,on} \left[d_i + (1 - d_i) \left(\frac{V_{pv,min}}{V_{dc}} \right)^2 \right] \\ B &= V_{pv,max} + V_{pv,min} + 2t_{tr} f_{sw} I_{pv,min} \left(1 + \frac{\Delta I_{ripple}}{2} \right) \\ &\quad - 2R_{DS,on} I_{pv,min} \left[d_i + (1 - d_i) \left(\frac{V_{pv,min}}{V_{dc}} \right)^2 \right] \\ C &= (V_{dc}^2 + V_{pv,min}^2) C_{oss} f_{sw} - V_{pv,max} I_{pv,max} - V_{pv,min} I_{pv,min} \\ &\quad + 2V_{GS}^2 C_{iss} f_{sw} + R_{DS,on} I_{pv,min}^2 \left[d_i + (1 - d_i) \left(\frac{V_{min}}{V_{dc}} \right)^2 \right] \\ &\quad - 2t_{tr} f_{sw} V_{pv,min} I_{pv,min} \left(1 + \frac{\Delta I_{ripple}}{2} \right) \end{aligned}$$

where V_{dc} is the output voltage of centralized boost converter, ΔI_{ripple} is the percentage current ripple, and d_i refers to the

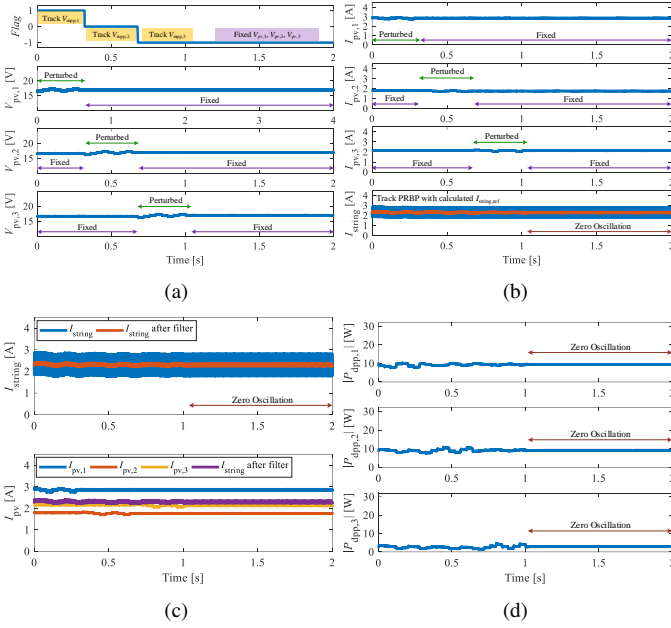


Fig. 7. Simulation results for stable shading scenarios. (a) Submodule voltage. (b) Submodule current. (c) I_{string} and filtered I_{string} . (d) Processing power distribution.

duty cycle for the primary side switch of the i^{th} BFC-based DPP converter.

Then, the related string current of PRBP could be delivered by solving (17), as

$$I_{PRBP} = \frac{-B \pm \sqrt{B^2 - 4AC}}{2A} \quad (18)$$

Besides, based on aforementioned analysis, I_{PRBP} is a unique solution located between $I_{pv,min}$ and $I_{pv,max}$. Hence, (11) could be rewritten with (18) as

$$I_{string,ref} = \frac{-B \pm \sqrt{B^2 - 4AC}}{2A} \quad (19)$$

where $I_{string,ref} \in [I_{pv,min}, I_{pv,max}]$. Once (19) obtained, control unit sends $I_{string,ref}$ to PI controller for centralized boost converter control. After regulated the string current, the differential power could be balanced.

IV. SIMULATION AND EXPERIMENTAL EVALUATIONS

A. Simulation Evaluations

A simulation evaluation with stable and dynamic irradiance conditions is carried out in PSIM for verifying the effectiveness of proposed IPRB control, including FSM-MPPT control for submodule power extraction and PRB control for string current regulation. The proposed control is verified with the aforementioned examples of three submodules and bidirectional flyback converters, as demonstrated in Fig. 3. The FSM-MPPT control and PRB control share the same PSIM/C-Block function as the control unit. The perturbation interval is set at 0.04s during the simulations.

1) *Stable Shading Scenario*: For evaluation with stable irradiance, three mismatched PV submodules are used with their irradiance level set as 0.8 kW/m^2 , 0.5 kW/m^2 and 0.6 kW/m^2 , respectively. The MPP currents respect to corresponding irradiance level are 2.8A, 1.75A, and 2.1A, respectively. The main simulation results are illustrated in Fig. 7. The

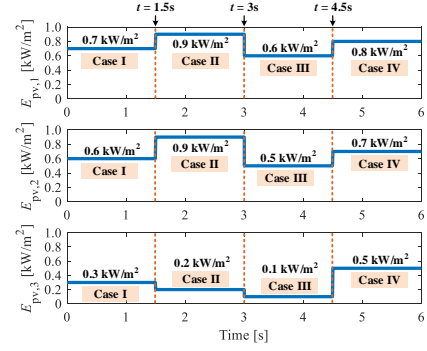


Fig. 8. Dynamic partial shading scenarios in simulation.

Flag signal and submodules output voltages are demonstrated in Fig. 7(a). The control unit tracks the MPP of submodule 1 while *Flag* equals to '1'. Meanwhile, the voltages of submodule 2 and 3 are fixed during this period. Once submodule 1 approached MPP operation, the voltage of submodule 1 is fixed, and *Flag* switches to '0' for tracking submodule 2. Then, the voltage of submodule 3 continues fixed until MPP of submodule 2 is approached, and *Flag* equals to '-1'. During the tracking process for the submodule 3, the voltage of submodule 1 and 2 are fixed. As illustrated in Fig. 7(a), all MPPs are successfully approached at around 1.1s with the implementation of proposed FSM-MPPT. The submodules currents and string current in the simulation are demonstrated in Fig. 7(b). Here, the filtered string current represents the string current after a first-order low pass filter, symbolizing the reference of string current. Notably, the fluctuation in string current could be mitigated by increasing the switching frequency [17]. As illustrates in Fig. 7(c), string current can be regulated to the middle between the extreme value of submodule currents, which refers to the PRB point of DPP converter operation. Fig. 7(d) shows the power distribution of each DPP converters. As the aforementioned theoretical analysis, the unit-maximum power distributions are balanced with the proposed IPRB control. All the results evaluated the performance of proposed control under stable irradiance conditions.

2) *Dynamic Shading Scenarios*: Dynamic partial shading scenarios for dynamic verification are set as demonstrated in Fig. 8. Notably, the irradiance for submodule 1 is marked with $E_{pv,1}$ is initially set at 0.7 kW/m^2 and increases to 0.9 kW/m^2 at $t = 1.5 \text{ s}$, then reduced to 0.6 kW/m^2 at $t = 3 \text{ s}$, and finally obtained at 0.8 kW/m^2 at $t = 4.5 \text{ s}$. The irradiance for submodule 2 is marked with $E_{pv,2}$ is initially set at 0.6 kW/m^2 and increases to 0.9 kW/m^2 at $t = 1.5 \text{ s}$, then decrease to 0.5 kW/m^2 at $t = 3 \text{ s}$ and finally approached and maintained at 0.7 kW/m^2 at $t = 4.5 \text{ s}$. For irradiance of submodule 3 marked with $E_{pv,3}$, it begins at 0.3 kW/m^2 and decreases to 0.2 kW/m^2 at $t = 1.5 \text{ s}$, then returns to 0.1 kW/m^2 at $t = 3 \text{ s}$, and finally increases to 0.5 kW/m^2 at $t = 4.5 \text{ s}$. With the changes in irradiance, four shading scenarios could be classified.

Theoretically, the maximum withstanding power stress in one DPP converter is the MPP power of the PV submodule by tracking LPP. Hence, the rated power of DPP converters should be at least designed to 60W for MSX-60 PV model, which

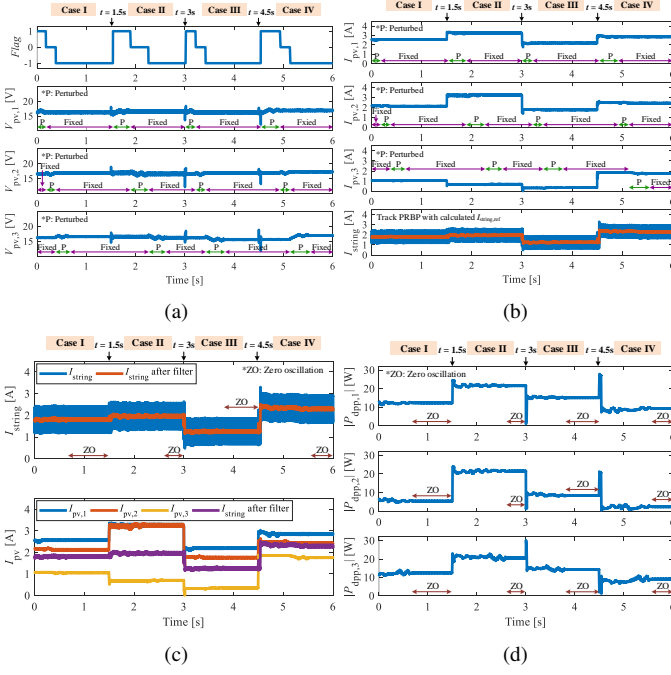


Fig. 9. Simulation results for dynamic shading scenarios. (a) Submodule voltage. (b) Submodule current. (c) I_{string} and filtered I_{string} . (d) Differential power distribution.

represents to the PSC that one submodule is fully shaded while the other two are with STC. Meanwhile, by operating at PRBP, the maximum differential power withstand in the DPP converters would be reduced to half of it with seeking LPP in the worst shading scenario. By considering the design margin, a higher region should be approached, which may reduce cost-effectiveness. Fig. 9 demonstrated the main simulation results with dynamic PSCs, includes the 'Flag' signal, PV voltage, PV current, string current and differential power. The 'Flag' signal and submodule voltages are illustrated in Fig. 9(a). With FSM-MPPT control, the MPP voltage of each PV submodules could successfully tracked in order. Once the MPP voltage of PV submodule 3 is obtained, the PV voltage regulation is fixed and switched into the zero oscillation state until the irradiance changed again. Fig. 9(b) illustrated the PV submodule currents and the string current under four shading scenarios. With proposed IPRB control, the optimal string current with variable PSCs follows the calculated reference value as 1.7765A, 1.9687A, 1.2681A, and 2.304A, respectively. Notably, the string current would also obtained the zero oscillation state according to fixed steady state submodule currents as drawn in Fig. 9(c). Hence, the distribution of unit-maximum differential power could be balanced by seeking the PRBP, as shown in Fig. 9(d).

B. Experimental Evaluations

An experimental platform built with three series-connected PV submodules, as in Fig. 3, is used to verify the performance of proposed control. The MSX-60 PV model is employed as the PV submodule, and the parameters are listed in TABLE II. The specifications of DPP converters and centralized boost converter are listed in TABLE IV, and experimental prototype is shown in Fig. 10(a). The dSPACE DS1104 module is used to install the proposed IPRB control. The electronic

TABLE IV
SYSTEM SPECIFICATIONS

Parameter	Symbol	Model and Value
Flyback converter switch	Q_{pri}, Q_{sec}	IRFP460
Flyback converter primary-side capacitor	C_{pri}	220 μ F
Flyback converter secondary-side capacitor	C_{sec}	47 μ F
Transformer magnetic inductor	L_{mg}	300 μ H
Transformer turns ratio	$N_{pri} : N_{sec}$	1:3
Boost converter switch	Q_{boost}	IRFP250
Boost converter diode	D	RHRG30120
Boost converter capacitor	C_{out}	47 μ F
Boost converter inductor	L	1mH
Switching frequency	f_{sw}	20kHz
Sampling interval in simulation	T_p (Sim.)	0.04s
Sampling interval in experiment	T_p (Exp.)	0.3s

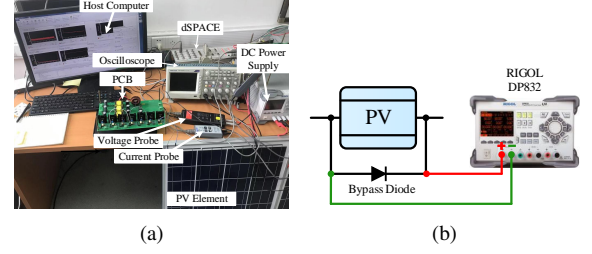


Fig. 10. Experimental prototype. (a) Experimental platform. (b) Connection for emulating irradiance level.

load, IT8514C+, is used and operates as a constant voltage load with a value of 100V. In order to simulate the PSCs accurately, the bias-current-injected method is introduced with a DC power supply, which operates at constant current (CC) mode. Hence, each submodule is parallel connected with the DC power supply RIGOL DP832 as illustrated in Fig. 10(b). The photocurrent could be approached by the output current of DP832, and emulates the actual irradiance level. Then, the emulation of partial shading is easily achieved by changing the output current of the relevant DC power supply. The sampling interval is set to 0.3s.

The proposed control is compared with the voltage equalization control by experiment, which is as a suboptimal MPPT solution. The measured power versus voltage curves under various irradiance levels for the MSX-60 PV model are demonstrated in Fig. 11(a). It indicates that the voltage deviation between the true MPPT line and VE line is easily occurred with irradiance variations, especially with a low irradiance level. Additionally, several factors would deteriorate the deviation, such as production tolerances, uneven aging degradation [50]–[53]. Basically, the P_{mpp} degradation is around 0.4% to 0.6% per year, mainly dominated by the decline of fill factor [53]. As reported by [52], the standard deviation of MPP voltage may increase by four times, and the MPP current may decrease 16.57% after 20 years. These types of degradation is undesired for voltage equalization implement, which would further deteriorate power loss. Hence, the individual MPPT operation should be employed for yielding the power extraction instead of VE control.

For quantifying the effect of voltage deviation due to irradiance variation, the measured percentage power loss due to voltage equalization θ_{VE} is induced and expressed as

$$\theta_{VE} = \left(1 - \frac{P_{VE}}{P_{MPPT}}\right) \times 100\% \quad (20)$$

where P_{VE} and P_{MPPT} are the maximum power ex-

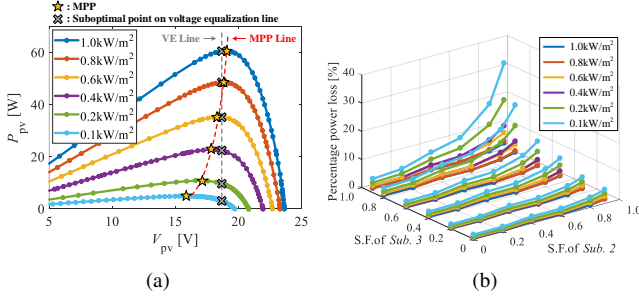


Fig. 11. Negativeness with voltage equalization. (a) Voltage shift against true MPP. (b) Percentage power loss with various PSCs.

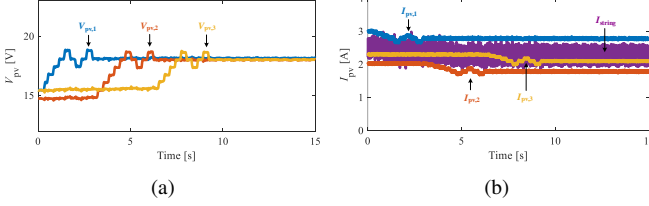


Fig. 12. Experimental results with steady irradiance. (a) Submodule voltage. (b) Submodules and string current.

traction with simplified voltage equalization and true MPPT control, respectively. In this test, submodule 1 is swept with 0.1kW/m², 0.2kW/m², 0.4kW/m², 0.6kW/m², 0.8kW/m², and 1.0kW/m². Submodule 2 and submodule 3 is swept with the shading factor of 0, 0.2, 0.4, 0.6, 0.8, and 0.9, respectively. The percentage power loss with variable PSCs is indicated in Fig. 11(b). It could be observed that the percentage power loss due to VE is increased with the exacerbation of partial shading. Notably, the potential power loss may approach 30% in some severe scenarios. In consideration of the occurrence frequency of PSC in the real world [30], it is necessary to employ a true MPPT rather than the suboptimal operation with simplified voltage equalization. Besides, the implementation of VE required a high similarity in PV parameters, which would reduce the capability of replacement parts.

In order to verify the effectiveness of proposed IPRB control, the experiments include steady and dynamic irradiance evaluations. As demonstrated in Fig. 12, the effectiveness of proposed IPRB control with steady PSC is verified. The irradiance of three submodules are set as in simulation with the value of 0.8kW/m², 0.5kW/m², and 0.6kW/m², respectively. The submodule voltages are illustrated in Fig. 12(a), and occurs obvious three-level perturbation while approached individual MPP. The submodule and string currents are shown in Fig. 12(b). Once the MPP of a specific submodule is obtained, the FSM-MPPT control switched to seek the MPP of the next submodule until all individual MPPs are approached and zero steady state oscillation in submodule level is achieved. With proposed IPRB control, the string current could be successfully maintained at the PRBP to balance the power distribution among DPP converters.

To validate the dynamic performance of proposed IPRB control, the experimental evaluation with various PSCs is carried out, and the shading scenarios are as used in the simulations. Fig. 13 demonstrated the experimental results of proposed control under dynamic PSCs. Similar to the results

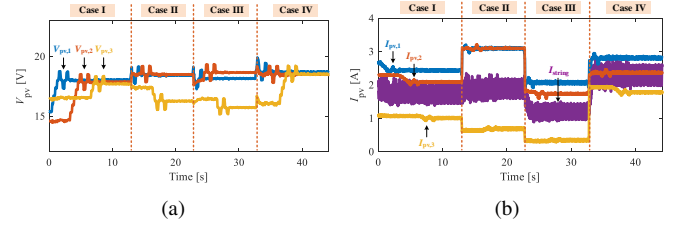


Fig. 13. Experimental results with dynamic irradiance. (a) Submodule voltage. (b) Submodules and string current.

with stable PSC, the submodule MPPs could be obtained in order by implementing the FSM-MPPT control. The string current quickly follows the changing shading scenarios and maintains at the deserved level with proposed PRB control, which as demonstrated in Fig. 13(b). Besides, zero oscillation is adopted in both of submodule- and module-level. Hence, the performance of proposed IPRB control is validated by both steady and dynamic PSCs.

C. Improvement with Proposed Control

The conventional PRB control shows some limitations in submodule- and/or module-level, such as control coupling, steady state oscillations, less cost-effectiveness for true MPP operations, and additional power loss. With the proposed IPRB control, several advances could be addressed and summarized as follows:

1) *Cost-effectiveness optimization*: A significant uneven power distribution may occur with LPPT controls in complicated mismatching scenarios, which would enhance the cost of DPP converters considering a reliable design redundancy. An even power distribution could reduce the unit-maximum power stress and the failure rate of switches in DPP converters by tracking the PRBP, which is beneficial to cost-effectiveness. Conventionally, distributed MPPT(DMPPT) is employed to obtain the submodule-level MPP [17], [19]. However, DMPPT required the parallel processing capability which is not available for a single-threaded microcontroller [54]. Thus, the implementation of DMPPT required multiple microcontrollers or multi-threading controller, which would induce additional cost. In [20], voltage equalization is induced and shows the effectiveness of solving control complexity. However, the practicability of VE technique is limited in the cases of uneven aging or the applications with different PV module specifications, which are required to be considered in-field operation. With the proposed FSM-MPPT control, the amount of MPPT controller could be reduced to one as with TS-MPPT or voltage equalization, considered its sequential processing characteristic. Besides, as the comparison demonstrated in Fig. 14, the limitation of VE could be eliminated but ensured a reliable tracking accuracy as with DMPPT.

2) *Control coupling reduction*: Traditionally, the control for the submodule and module level are separated from each other, as in [17] and [19]. However, the implementation of two extreme-seeking algorithm increases monolithic control coupling [20]. Notably, multiple module-level regulations are required to be embedded in each submodule MPPT perturbation step, as demonstrated in Fig. 14(a). In the experimental validations of [17] and [19], the perturbation time

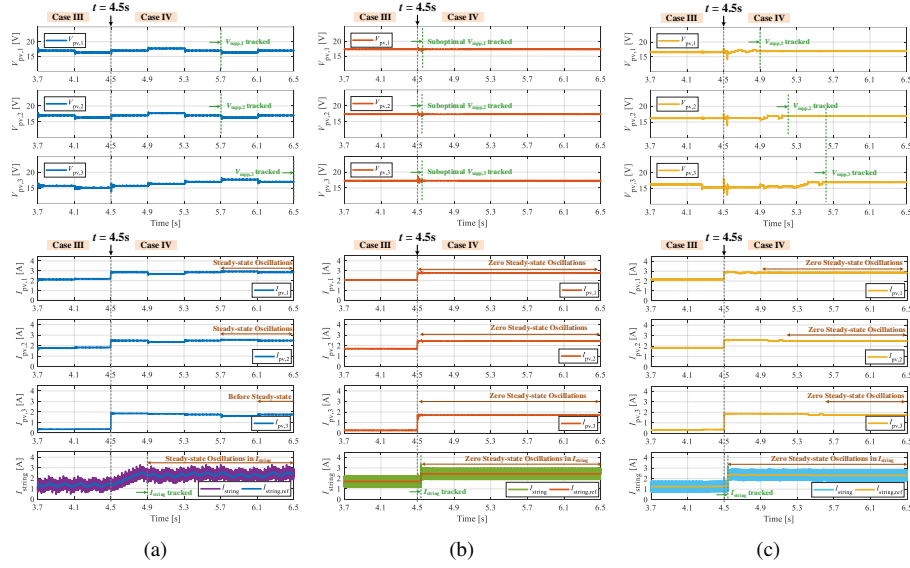


Fig. 14. Comparison between various controls under the step-changing shading conditions from Case III to Case IV. (a) UM-LPPT in [19]. (b) VE-based PRB in [20]. (c) Proposed IPRB.

for submodule MPPT is selected at 10s to obtain a stable operation with the optimal point in module level, which would significantly reduce the dynamic response of MPPT control. Moreover, the coordination between submodule and module-level control enhances the complexity and coupling level and leads to the potential tracking error with some mismatching scenarios. With proposed IPRB, the control coupling could be reduced by synchronizing the current value referred to PRBP while seeking the submodule MPPs. The determination of string current reference in proposed control is integrated with FSM-MPPT and shared the same control unit. As illustrated in Fig. 14(c), the $I_{string,ref}$ follows the change in each sample interval show a higher dynamic with proposed IPRB control than that with UM-LPPT in Fig. 14(a). Thus, the control coupling between submodule- and module-level control could be reduced.

3) *Oscillations elimination*: The oscillations in output power are mainly caused by the multiple extreme-seeking controls, which may induce external power loss. As demonstrated in Fig. 14(a), steady-state oscillation is existed in both submodule and module-level control with conventional PRB control, as UM-LPPT, in [19]. Besides, the asynchronous perturbation time would slow down the dynamic response to the rapid change in irradiance. As specified in Fig. 14(c), the I_{string} regulation could be significantly improved with the implementation of proposed control, which is with synchronous perturbation. Meanwhile, the proposed control could eliminate the steady-state oscillations once the submodule MPPs are tracked. Notably, as illustrated in Fig. 14(b), the VE-based solution [20] could obtain the zero oscillation as that with the proposed control. However, voltage equalization has its limitations in suboptimal MPP operation, which increased the system power loss. Also, VE is not suitable for the PV module uncertainty, and the equalized voltage might shift from actual MPP with specifications variation.

V. RELIABILITY IN PV-TO-BUS DPP ARCHITECTURES

A. Basic Concept of Component Failure Rate Analysis

It is well known that the power stress of DPP converters will affect their lifetime. In order to quantify the influence due to the power distribution, component-level reliability analysis is carried out considering that the failure rate or hazard rate, λ , is an important metric to quantify the engineering reliability [55]. The component-level reliability analysis will focus on the failure rate of key electrical components, including power semiconductors, capacitors, and magnetic devices by using widely recognized empirical models in the military handbook for the reliability prediction of electronic equipment (MIL-HDBK-217) [47], [56], [57]. With the component-level reliability analysis, the system failure rate λ_{sys} in units per million hours is expressed by

$$\lambda_{sys} = \lambda_{sw} + \lambda_C + \lambda_{TR} \quad (21)$$

where λ_{sw} , λ_C , λ_{TR} refers to failure rate of power MOSFETs, capacitors and transformers, respectively.

Specifically, for N-channel MOSFETs, λ_{sw} can be expressed as:

$$\lambda_{sw} = \lambda_{b,sw} \pi_T \pi_A \pi_Q \pi_E \quad (22)$$

where $\lambda_{b,sw}$, π_T , π_A , π_Q , π_E represents the basic failure rate of MOSFETs, temperature factor, application factor, quality factor and environment factor, respectively.

Normally, $\lambda_{b,sw}$ is constant, which is 0.012 for MOSFET [58]. π_A , π_Q and π_E are 8, 8 and 1, respectively. π_T is expressed by

$$\pi_T = \exp \left[-1925 \left(\frac{1}{T_J + 273} - \frac{1}{298} \right) \right] \quad (23)$$

where T_A is the ambient temperature. T_J is the junction temperature and can be expressed as " $T_J = T_A + \theta_{JA} P_{sw}$ ". θ_{JA} is junction-to-ambient thermal resistance.

The failure rate of transformers λ_{TR} can be calculated by

$$\lambda_{TR} = \lambda_{b,TR} \pi_Q \pi_E \quad (24)$$

where the basic failure rate for transformers, $\lambda_{b,TR}$, is set as 0.0028 with an operating temperature at 40°C.

For the electrolytic capacitor, the failure rate λ_C can be calculated by

$$\lambda_C = \lambda_{b,C} \pi_{CV} \pi_Q \pi_E \quad (25)$$

where π_Q is set as 1, π_{CV} is the capacitance factor and expressed as $\pi_{CV} \approx 0.34C^{0.18}$, V_{op} is the operating voltage, V_{rated} is the rated voltage. $\pi_{b,C}$ can be expressed by

$$\pi_{b,C} = 0.00254 \left[\left(\frac{2V_{op}}{V_{rated}} \right)^3 + 1 \right] \exp \left[5.09 \left(\frac{T_A + 273}{358} \right)^5 \right] \quad (26)$$

B. Component Failure Rate Analysis in PV-to-Bus DPP Architectures

In this paper, a PV-to-bus DPP architecture with three MSX-60 PV submodules is adopted for the analysis and Fig. 3(a) illustrates the system diagram, where the bidirectional flyback converter (BFC) and the boost converter are selected as the DPP converter and centralized converter, as shown in Fig. 3(b) and Fig. 3(c), respectively. Based on the above-discussed component-failure-rate based reliability method, the failure rate of i^{th} BFC λ_{BFC_i} can be expressed as:

$$\lambda_{BFC_i} = \lambda_{sw_{pri,i}} + \lambda_{sw_{sec,i}} + \lambda_{TR_i} + \lambda_{C_{pri,i}} + \lambda_{C_{sec,i}} \quad (27)$$

The failure rate of transformers and capacitors in the PV-to-bus DPP architecture can be approximated as constants. Thus, λ_{sw} becomes the key factor that affects the total failure rate of the BFC-based DPP converter, which is changing with the processed power. With the discussions above, the tracking of LPP and PRBP will affect the power distribution in DPP converters, which further affects the system failure rate. Hence, a fair comparison of the failure rate in the PV-to-bus DPP architecture by using LPPT, VE-based PRB and proposed IPRB control is conducted to show the function of different strategies in DPP converters.

For BFCs, the primary and secondary side devices are IRFP460 [18] and the component specifications f_{sw} , V_{GS} , θ_{JA} , $R_{DS,on}$, t_{tr} , C_{iss} , C_{oss} are set as 20kHz, 15V, 40°C/W, 0.27Ω, 59ns, 4200pF and 870pF, respectively [59]. The voltage of DC bus, V_{dc} , is set to 100V, which is the voltage stress on the secondary-side power devices.

For the centralized boost converter, the corresponding failure rate, λ_{boost} , could be expressed as:

$$\lambda_{boost} = \lambda_{sw,boost} + \lambda_D + \lambda_L + \lambda_{C_{out}} \quad (28)$$

where, $\lambda_{sw,boost}$, λ_D , λ_L and $\lambda_{C_{out}}$ represent the failure rate of the power device, diode, inductor and output capacitor, respectively.

Similar as the analysis in BFCs, the component-failure-rate based reliability assessment for the centralized boost converter can be mainly focused on the power switch Q_{boost} and the corresponding failure rate expression is shown in (22). The main power switch is IRFP250 [18] and the component specifications f_{sw} , V_{GS} , θ_{JA} , $R_{DS,on}$, t_{tr} , C_{iss} , C_{oss} are set as 20kHz, 15V, 40°C/W, 0.075Ω, 43ns, 2159pF and 315pF, respectively [60].

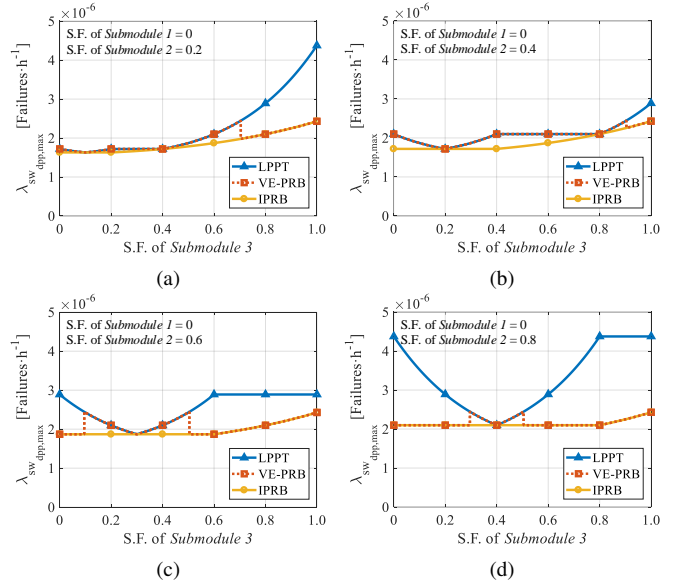


Fig. 15. The impact of controls on maximum failure rate in DPP converters $\lambda_{sw_{dpp,max}}$ under various shading factor of submodule 3. (a) S.F.₁ = 0 and S.F.₂ = 0.2. (b) S.F.₁ = 0 and S.F.₂ = 0.4. (c) S.F.₁ = 0 and S.F.₂ = 0.6. (d) S.F.₁ = 0 and S.F.₂ = 0.8.

Thus, the system reliability of the PV-to-Bus DPP architecture, λ_{sys} , could be evaluated by considering both the failure rate of DPP converters λ_{BFC_i} and boost converter λ_{boost} , which can be expressed as:

$$\begin{aligned} \lambda_{sys} &= \lambda_{boost} + \sum_{i=1}^n \lambda_{BFC_i} \\ &\simeq \lambda_{sw,boost} + \sum_{i=1}^n \lambda_{sw_{pri,i}} + \sum_{i=1}^n \lambda_{sw_{sec,i}} \end{aligned} \quad (29)$$

Taking the reliability assessment of BFCs under various shading conditions as the example, the calculated λ_{sw} concerning the shading factor of submodule 3 is illustrated in Fig. 15. The solar irradiance with a S.F. = 0 is set at 1.0kW/m², and the ambient temperature T_A is set as 25°C for the standard test condition (STC) operation. The designed power rating of DPP converter equals to half of the MSX-60 PV module MPP power with STC, as 30W. As illustrated in Fig. 15, the proposed IPRB can effectively reduce the maximum failure rate of the power switches among DPP converters $\lambda_{sw_{dpp,max}}$ compared with LPPT [17], [18] and VE-PRB [20] control, which is consistent with the power distribution in Fig. 4. Notably, the proposed IPRB control illustrated lower failure rates within the designed rating of DPP converters. Thus, $\lambda_{sw_{dpp,max}}$ can be reduced by using the proposed IPRB with the reduced power stress endured in DPP converters.

C. Mission Profile-based Reliability Assessment

In the real world, the environmental conditions would not be constant considering the substantial variation in the irradiance and ambient temperature. Thus, it is necessary to adopt the mission profile in the system reliability analysis [61]–[64]. Hence, the mission profile-based reliability assessment is employed to evaluate the impact of controls on the reliability under meteorological conditions. Fig. 16 demonstrated the yearly mission-profiles (i.e., irradiance and ambient temperature with a sampling resolution of one-minute) in University of Nevada, Las Vegas (UNLV), Las Vegas, NV, USA, 2019.

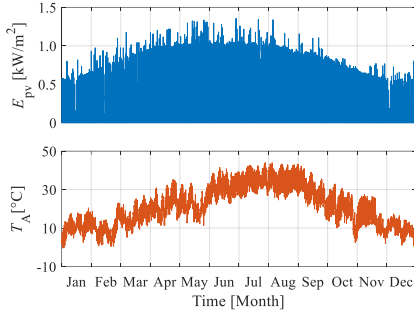


Fig. 16. Yearly mission profiles (i.e., irradiance and ambient temperature with a sampling resolution of one-minute) in University of Nevada, Las Vegas (UNLV), Las Vegas, NV, USA, 2019.

The comparisons in terms of failure rate and reliability are carried out under several different shading scenarios, includes light-, medium- and severe-shaded conditions. The detailed shading scenarios are defined as:

- Light-shaded scenario: $S.F._1 = 0$, $S.F._2 = 0$, $S.F._3 = 0.7$
- Medium-shaded scenario: $S.F._1 = 0$, $S.F._2 = 0.2$, $S.F._3 = 0.8$
- Severe-shaded scenario: $S.F._1 = 0$, $S.F._2 = 0.7$, $S.F._3 = 0.9$

Here, $S.F._1$, $S.F._2$, and $S.F._3$ refer to the shading factor of PV submodule 1, 2 and 3, respectively. The designed power rating of DPP converter is set at 42W, which is considered with the peak irradiance among the mission profiles. Notably, the transient state would be ignored in this analysis, considering that irradiance variations are much longer than the dynamic response of different controls. As demonstrated in Fig. 17, the total differential power $P_{dpp,tot}$ by implementing IPRB is lightly higher than that with LPPT under three shading conditions. Meanwhile, the local enlarged image illustrated that VE-PRB would switch between the LPP and PRB, which is DPP converter power rating depended. Notably, the maximum power stress $P_{dpp,max}$ by using the IPRB is lower than with LPPT and is fractionally approached the power stress with LPPT, which is highly relevant to the failure rate in three DPP converters. With the same power switch specifications, proposed IPRB illustrated the lower total power loss in DPP converters $P_{sw,tot}$ compared with other controls in Fig. 17, and it is beneficial for the system efficiency. The impact of power loss on the junction temperature of both-side switches withstood $P_{dpp,max}$ are marked with $T_{J,pri}$ and $T_{J,sec}$. The operation with proposed IPRB contributes to a lower junction temperature due to the lower power loss in the stressful power switches. With higher power stress in the single DPP converter, the maximum failure rate among switches of DPP converters $\lambda_{swdpp,max}$ is higher with LPPT or VE-PRB controls, which is undesirable for system lifetime. Moreover, the uneven power distribution leads to the higher design requirements of the DPP converter, reducing cost-effectiveness. For instance, the designed power rating with LPPT should meet the MPP power extraction of PV submodule at STC by considering the worst shading case during the operation. Alternatively, the designed power could be reduced to the half of MPP power with VE-PRB or proposed IPRB control.

The impact of different controls on the failure rate of

centralized boost converter is validated in Fig. 18. The power processed by boost converter P_{boost} demonstrated a negative correlation with the shading level. Thus, the power loss $P_{sw,boost}$ would decreased in boost converter with the increasing shading level. Accordingly, the power processed by boost converter and power loss in switch with proposed IPRB control is slightly lower than that with LPPT or VE-PRB control, which is benefit to the reliability enhancement with investigated light- or medium-shaded scenarios. The junction temperature of power switch showed positive correlation with the power loss in a centralized boost converter, which shows a lower $T_{J,boost}$ in these two PSCs. Notably, as illustrated in Fig. 19(c), the lower processing power in boost converter occurred with LPPT control with the severe-shaded scenario, which further introduces a lower failure rate.

The failure rate in DPP converters and boost converter did not show the same trend among three shading scenarios. Thus, the system-level failure rate λ_{sys} in (29) is introduced to investigate the impact of different controls. Compared with LPPT and VE-PRB, the proposed IPRB control performed a lower failure rate under the mission profiles, as illustrated in Fig. 19. For further quantitative analysis of reliability impact, the system reliability $R(t)$ is introduced to investigate the effect of failure rate variation with yearly mission profiles, which is expressed as [28]:

$$R(t) = e^{-\int \lambda_{sys} dt} = e^{-\lambda_{sys} t} \quad (30)$$

Based on the failure rate of DPP architecture, the system reliability variations after the yearly mission-profiles operation could be demonstrated as in Fig. 20 under the three investigated PSCs. The system reliability could be maintained at the slightly higher level with the proposed IPRB control after a one-year operation, which shows the advances of proposed control in reliability enhancement.

VI. CONCLUSION

In this paper, an improved power rating balancing control is proposed with the PV-to-bus DPP architecture using in DC microgrid. By employing the proposed control, the individual MPPs could be achieved by FSM-MPPT at the submodule level, which can improve the power yielding from PV submodule. The implement of FSM-MPPT control reduces the number of the control unit to one, which can further reduce the system cost. Besides, the proposed IPRB control provides a simple proof to approach an even unit-maximum power distribution by regulating the string current to the desired value based on the mathematical analysis of power delivery with non-ideal characteristic consideration. The simulations and experimental results verify the effectiveness of proposed IPRB control under steady and dynamic shading conditions.

VII. ACKNOWLEDGMENT

This work was supported by the Research development fund of XJTLU (RDF-17-01-28), the Research Enhancement fund of XJTLU (REF-17-01-02), the Suzhou Prospective Application programme (SYG202016), and the XJTLU Key Programme Special Fund (KSF-A-08, KSF-E-13, KSF-T-04).

Yinxiao Zhu, Huiqing Wen, Guanying Chu, Xue Wang and Qilin Peng are with the School of Advanced

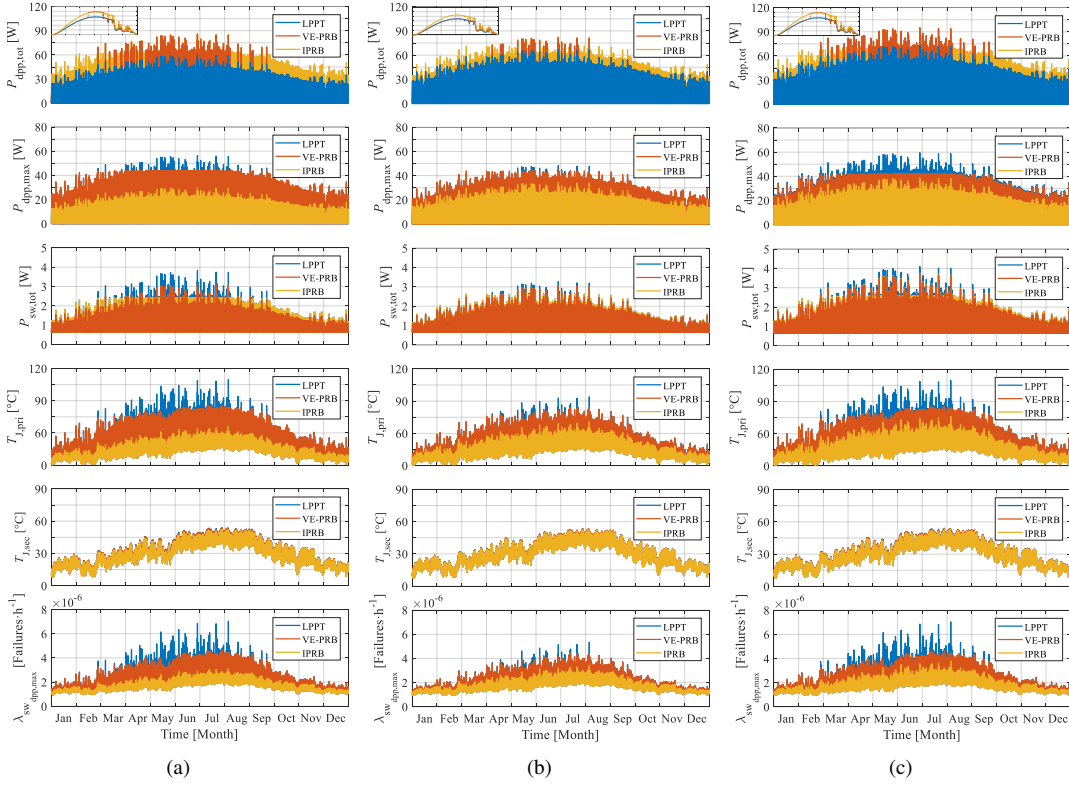


Fig. 17. The impact of controls on DPP converters with various shading conditions under yearly mission-profiles. (a) Light-shaded scenario. (b) Medium-shaded scenario. (c) Severe-shaded scenario.

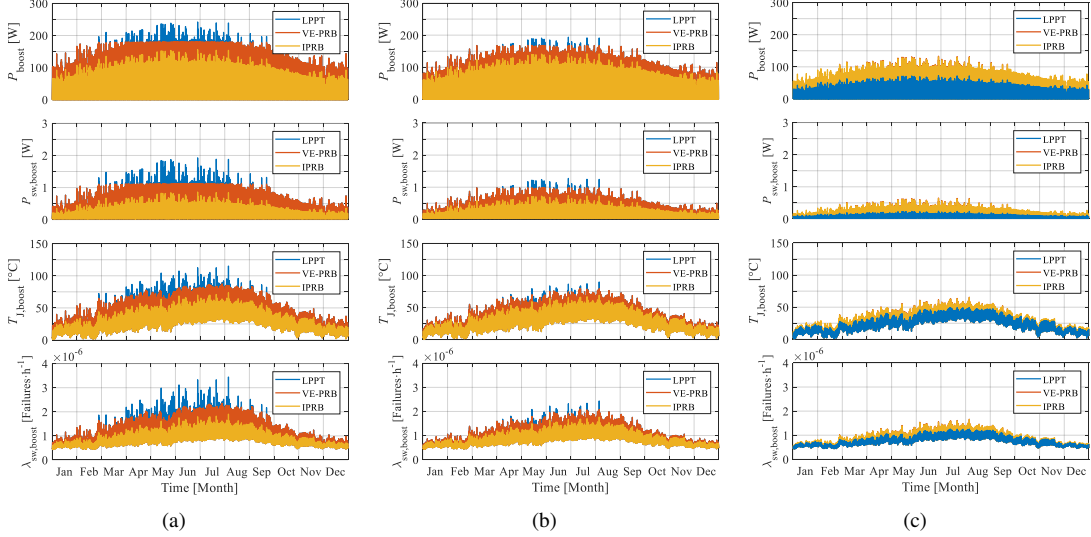


Fig. 18. The impact of controls on centralized boost converter with various shading conditions under yearly mission-profiles. (a) Light-shaded scenario. (b) Medium-shaded scenario. (c) Severe-shaded scenario.

Technology, Xi'an Jiaotong-Liverpool University, Suzhou 215123, China (e-mail: Yinxiao.Zhu19@student.xjtlu.edu.cn; Huiqing.Wen@xjtlu.edu.cn; Guanying.Chu@xjtlu.edu.cn; Xue.Wang19@student.xjtlu.edu.cn).

Yihua Hu is with the University of York, York YO10 5DD, U.K. (e-mail: yihua.hu@york.ac.uk).

Lin Jiang is with the University of Liverpool, Liverpool L69 3BX, U.K. (e-mail: l.jiang@liverpool.ac.uk).

REFERENCES

- [1] P. Benalcázar, J. Lara, and M. Samper, "Distributed photovoltaic generation in ecuador: Economic analysis and incentives mechanisms," *IEEE Latin America Transactions*, vol. 18, no. 03, pp. 564–572, 2020.
- [2] T. Georgitsioti, N. Pearsall, and I. Forbes, "Simplified levelised cost of the domestic photovoltaic energy in the uk: the importance of the feed-in tariff scheme," *IET Renewable Power Gener.*, vol. 8, no. 5, pp. 451–458, 2014.
- [3] M. Yao and X. Cai, "An overview of the photovoltaic industry status and perspective in china," *IEEE Access*, vol. 7, pp. 181 051–181 060, 2019.
- [4] B. Sun, Y. Yu, and C. Qin, "Should china focus on the distributed development of wind and solar photovoltaic power generation? a comparative study," *Appl. Energy*, vol. 185, pp. 421–439, Jan 2017.
- [5] P. Dong, H. Wen, G. Chu, Y. Yang, and Y. Wang, "Power rating analysis and protection for photovoltaic-isolated port based differential power processing systems," *Sol. Energy*, vol. 193, pp. 458–472, Nov 2019.
- [6] Z. Moradi-Shahrababak, A. Tabesh, and G. R. Yousefi, "Economical design of utility-scale photovoltaic power plants with optimum availabil-

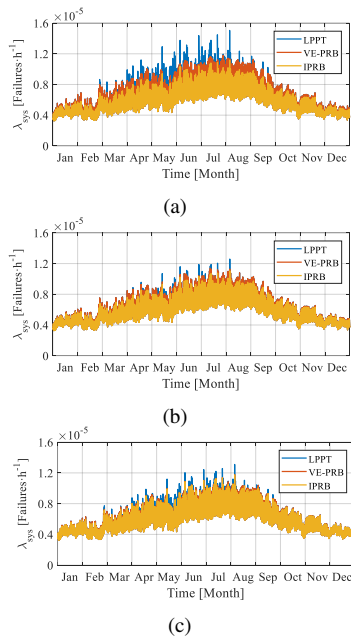


Fig. 19. The impact of controls on the system failure rate of three submodule-based PV-bus DPP architecture with various shading conditions under yearly mission-profiles. (a) Light-shaded scenario. (b) Medium-shaded scenario. (c) Severe-shaded scenario.

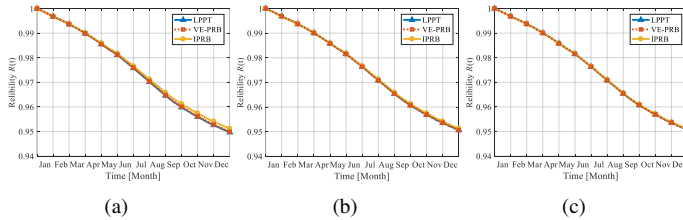


Fig. 20. The impact of controls on the reliability of three submodule-based PV-bus DPP architecture with various shading conditions under yearly mission-profiles. (a) Light-shaded scenario. (b) Medium-shaded scenario. (c) Severe-shaded scenario.

ity,” *IEEE Trans. Ind. Electron.*, vol. 61, no. 7, pp. 3399–3406, 2014.

- [7] E. Koutroulis and F. Blaabjerg, “Design optimization of transformerless grid-connected pv inverters including reliability,” *IEEE Trans. Power Electron.*, vol. 28, no. 1, pp. 325–335, 2013.
- [8] M. Alramlawi and P. Li, “Design optimization of a residential pv-battery microgrid with a detailed battery lifetime estimation model,” *IEEE Trans. Ind. Appl.*, vol. 56, no. 2, pp. 2020–2030, 2020.
- [9] C. S. Lai and M. D. McCulloch, “Sizing of stand-alone solar pv and storage system with anaerobic digestion biogas power plants,” *IEEE Trans. Ind. Electron.*, vol. 64, no. 3, pp. 2112–2121, 2017.
- [10] A. B. Acharya, M. Ricco, D. Sera, R. Teodorescu, and L. E. Norum, “Performance analysis of medium-voltage grid integration of pv plant using modular multilevel converter,” *IEEE Trans. Energy Convers.*, vol. 34, no. 4, pp. 1731–1740, 2019.
- [11] N. Agarwal, A. Arya, M. W. Ahmad, and S. Anand, “Lifetime monitoring of electrolytic capacitor to maximize earnings from grid-feeding pv system,” *IEEE Trans. Ind. Electron.*, vol. 63, no. 11, pp. 7049–7058, 2016.
- [12] P. D. Reigosa, H. Wang, Y. Yang, and F. Blaabjerg, “Prediction of bond wire fatigue of igbts in a pv inverter under a long-term operation,” *IEEE Trans. Power Electron.*, vol. 31, no. 10, pp. 7171–7182, 2016.
- [13] A. Mäki and S. Valkealahti, “Power losses in long string and parallel-connected short strings of series-connected silicon-based photovoltaic modules due to partial shading conditions,” *IEEE Trans. Energy Convers.*, vol. 27, no. 1, pp. 173–183, Mar 2012.
- [14] X. Li, H. Wen, Y. Hu, L. Jiang, and W. Xiao, “Modified beta algorithm for gmptt and partial shading detection in photovoltaic systems,” *IEEE Trans. Power Electron.*, vol. 33, no. 3, pp. 2172–2186, 2018.
- [15] M. Kermadi, Z. Salam, J. Ahmed, and E. M. Berkouk, “An effective hybrid maximum power point tracker of photovoltaic arrays for complex partial shading conditions,” *IEEE Trans. Ind. Electron.*, vol. 66, no. 9, pp. 6990–7000, 2019.
- [16] M. A. Ghasemi, H. M. Foroushani, and F. Blaabjerg, “Marginal power-based maximum power point tracking control of photovoltaic system under partially shaded condition,” *IEEE Trans. Power Electron.*, vol. 35, no. 6, pp. 5860–5872, 2020.
- [17] Y. Jeon, H. Lee, K. A. Kim, and J. Park, “Least power point tracking method for photovoltaic differential power processing systems,” *IEEE Trans. Power Electron.*, vol. 32, no. 3, pp. 1941–1951, Mar 2017.
- [18] G. Chu, H. Wen, Y. Yang, and Y. Wang, “Elimination of photovoltaic mismatching with improved submodule differential power processing,” *IEEE Trans. Ind. Electron.*, vol. 67, no. 4, pp. 2822–2833, 2020.
- [19] Y. Jeon and J. Park, “Unit-minimum least power point tracking for the optimization of photovoltaic differential power processing systems,” *IEEE Trans. Power Electron.*, vol. 34, no. 1, pp. 311–324, Jan 2019.
- [20] G. Chu, H. Wen, Y. Hu, L. Jiang, Y. Yang, and Y. Wang, “Low-complexity power balancing point-based optimization for photovoltaic differential power processing,” *IEEE Trans. Power Electron.*, vol. 35, no. 10, pp. 10 306–10 322, 2020.
- [21] R. C. N. Pilawa-Podgurski and D. J. Perreault, “Submodule integrated distributed maximum power point tracking for solar photovoltaic applications,” *IEEE Trans. Power Electron.*, vol. 28, no. 6, pp. 2957–2967, Jun 2013.
- [22] N. Pragallapati and V. Agarwal, “Distributed pv power extraction based on a modified interleaved sepic for nonuniform irradiation conditions,” *IEEE J. Photovolt.*, vol. 5, no. 5, pp. 1442–1453, Sep 2015.
- [23] O. Khan, W. Xiao, and H. H. Zeineldin, “Gallium-nitride-based submodule integrated converters for high-efficiency distributed maximum power point tracking PV applications,” *IEEE Trans. Ind. Electron.*, vol. 63, no. 2, pp. 966–975, Feb 2016.
- [24] F. Wang, T. Zhu, F. Zhuo, H. Yi, S. Shi, and X. Zhang, “Analysis and optimization of flexible mppt strategy in submodule pv application,” *IEEE Trans. Sustain. Energy*, vol. 8, no. 1, pp. 249–257, Jan 2017.
- [25] S. Sajadian and R. Ahmadi, “Distributed maximum power point tracking using model predictive control for photovoltaic energy harvesting architectures based on cascaded power optimizers,” *IEEE J. Photovolt.*, vol. 7, no. 3, pp. 849–857, May 2017.
- [26] O. Khan and W. Xiao, “Review and qualitative analysis of submodule-level distributed power electronic solutions in PV power systems,” *Renewable Sustainable Energy Rev.*, vol. 76, pp. 516–528, Sep 2017.
- [27] K. A. Kim, P. S. Shenoy, and P. T. Krein, “Converter rating analysis for photovoltaic differential power processing systems,” *IEEE Trans. Power Electron.*, vol. 30, no. 4, pp. 1987–1997, Apr 2015.
- [28] P. S. Shenoy, K. A. Kim, B. B. Johnson, and P. T. Krein, “Differential power processing for increased energy production and reliability of photovoltaic systems,” *IEEE Trans. Power Electron.*, vol. 28, no. 6, pp. 2968–2979, Jun 2013.
- [29] P. S. Shenoy and P. T. Krein, “Differential power processing for dc systems,” *IEEE Trans. Power Electron.*, vol. 28, no. 4, pp. 1795–1806, April 2013.
- [30] S. Qin, S. T. Cady, A. D. Domínguez-García, and R. C. N. Pilawa-Podgurski, “A distributed approach to maximum power point tracking for photovoltaic submodule differential power processing,” *IEEE Trans. Power Electron.*, vol. 30, no. 4, pp. 2024–2040, Apr 2015.
- [31] S. Qin, C. B. Barth, and R. C. N. Pilawa-Podgurski, “Enhancing microinverter energy capture with submodule differential power processing,” *IEEE Trans. Power Electron.*, vol. 31, no. 5, pp. 3575–3585, May 2016.
- [32] F. Wang, T. Zhu, F. Zhuo, and H. Yi, “An improved submodule differential power processing-based pv system with flexible multi-mppt control,” *IEEE Journal of Emerging and Selected Topics in Power Electronics*, vol. 6, no. 1, pp. 94–102, Mar 2018.
- [33] J. T. Stauth, M. D. Seeman, and K. Kesarwani, “Resonant switched-capacitor converters for sub-module distributed photovoltaic power management,” *IEEE Trans. Power Electron.*, vol. 28, no. 3, pp. 1189–1198, March 2013.
- [34] A. Blumenfeld, A. Cervera, and M. M. Peretz, “Enhanced differential power processor for pv systems: Resonant switched-capacitor gyrator converter with local mppt,” *IEEE Journal of Emerging and Selected Topics in Power Electronics*, vol. 2, no. 4, pp. 883–892, Dec 2014.
- [35] M. K. Al-Smadi and Y. Mahmoud, “Image-based differential power processing for photovoltaic microinverter,” *IEEE Trans. Energy Convers.*, pp. 1–1, 2020.
- [36] Y. Levron, D. R. Clement, B. Choi, C. Olalla, and D. Maksimovic, “Control of submodule integrated converters in the isolated-port differential power-processing photovoltaic architecture,” *IEEE Journal of Emerging and Selected Topics in Power Electronics*, vol. 2, no. 4, pp. 821–832, Dec 2014.
- [37] C. Olalla, C. Deline, D. Clement, Y. Levron, M. Rodriguez, and D. Maksimovic, “Performance of power-limited differential power processing

- architectures in mismatched pv systems," *IEEE Trans. Power Electron.*, vol. 30, no. 2, pp. 618–631, Feb 2015.
- [38] R. Bell and R. C. N. Pilawa-Podgurski, "Decoupled and distributed maximum power point tracking of series-connected photovoltaic submodules using differential power processing," *IEEE Journal of Emerging and Selected Topics in Power Electronics*, vol. 3, no. 4, pp. 881–891, Dec 2015.
- [39] G. Chu, H. Wen, L. Jiang, Y. Hu, and X. Li, "Bidirectional flyback based isolated-port submodule differential power processing optimizer for photovoltaic applications," *Sol. Energy*, vol. 158, pp. 929–940, Dec 2017.
- [40] C. Olalla, D. Clement, M. Rodriguez, and D. Maksimovic, "Architectures and control of submodule integrated dc–dc converters for photovoltaic applications," *IEEE Trans. Power Electron.*, vol. 28, no. 6, pp. 2980–2997, Jun 2013.
- [41] K. Sun, Z. Qiu, H. Wu, and Y. Xing, "Evaluation on high-efficiency thermoelectric generation systems based on differential power processing," *IEEE Trans. Ind. Electron.*, vol. 65, no. 1, pp. 699–708, Jan 2018.
- [42] H. Jeong, S. Park, J. H. Jung, T. Kim, A. R. Kim, and K. A. Kim, "Segmented differential power processing converter unit and control algorithm for photovoltaic systems," *IEEE Trans. Power Electron.*, vol. 36, no. 7, pp. 7797–7809, 2021.
- [43] M. Uno and A. Kukita, "Single-switch voltage equalizer using multistacked buck–boost converters for partially shaded photovoltaic modules," *IEEE Trans. Power Electron.*, vol. 30, no. 6, pp. 3091–3105, 2015.
- [44] M. Uno and A. Kukita, "Current sensorless equalization strategy for a single-switch voltage equalizer using multistacked buck–boost converters for photovoltaic modules under partial shading," *IEEE Trans. Ind. Appl.*, vol. 53, no. 1, pp. 420–429, 2017.
- [45] M. Uno and K. Honda, "Panel-to-substring differential power processing converter with embedded electrical diagnosis capability for photovoltaic panels under partial shading," *IEEE Trans. Power Electron.*, pp. 1–1, 2021.
- [46] H. Jeong, H. Lee, Y.-C. Liu, and K. A. Kim, "Review of differential power processing converter techniques for photovoltaic applications," *IEEE Trans. Energy Convers.*, vol. 34, no. 1, pp. 351–360, 2019.
- [47] D. Hirschmann, D. Tissen, S. Schroder, and R. W. D. Doncker, "Reliability prediction for inverters in hybrid electrical vehicles," *IEEE Trans. Power Electron.*, vol. 22, no. 6, pp. 2511–2517, Nov 2007.
- [48] M. Arifujjaman, M. T. Iqbal, and J. E. Quaicoe, "A comparative study of the reliability of the power electronics in grid connected small wind turbine systems," in *2009 Canadian Conference on Electrical and Computer Engineering*, 2009, pp. 394–397.
- [49] S. Yang, A. Bryant, P. Mawby, D. Xiang, L. Ran, and P. Tavner, "An industry-based survey of reliability in power electronic converters," *IEEE Trans. Ind. Appl.*, vol. 47, no. 3, pp. 1441–1451, 2011.
- [50] G. Cipriani, V. Di Dio, A. Marcotulli, and R. Miceli, "Manufacturing tolerances effects on pv array energy production," in *2014 International Conference on Renewable Energy Research and Application (ICRERA)*, 2014, pp. 952–957.
- [51] F. Spertino and J. S. Akilimali, "Are manufacturing $i-v$ mismatch and reverse currents key factors in large photovoltaic arrays?" *IEEE Trans. Ind. Electron.*, vol. 56, no. 11, pp. 4520–4531, 2009.
- [52] C. E. Chamberlin, M. A. Rocheleau, M. W. Marshall, A. M. Reis, N. T. Coleman, and P. A. Lehman, "Comparison of pv module performance before and after 11 and 20 years of field exposure," in *2011 37th IEEE Photovoltaic Specialists Conference*, 2011, pp. 000 101–000 105.
- [53] D. C. Jordan, B. Sekulic, B. Marion, and S. R. Kurtz, "Performance and aging of a 20-year-old silicon pv system," *IEEE J. Photovolt.*, vol. 5, no. 3, pp. 744–751, 2015.
- [54] S. Zouaoui, L. Boussaid, and A. Mtibaa, "Smallrtos: Microcontroller-based embedded multitasking," in *2017 International Conference on Engineering MIS (ICEMIS)*, 2017, pp. 1–6.
- [55] K. Ma, H. Wang, and F. Blaabjerg, "New approaches to reliability assessment: Using physics-of-failure for prediction and design in power electronics systems," *IEEE Power Electron. Mag.*, vol. 3, no. 4, pp. 28–41, 2016.
- [56] Y. Song and B. Wang, "Survey on reliability of power electronic systems," *IEEE Trans. Power Electron.*, vol. 28, no. 1, pp. 591–604, Jan 2013.
- [57] M. A. Masrur, "Penalty for fuel economy— system level perspectives on the reliability of hybrid electric vehicles during normal and graceful degradation operation," *IEEE Syst. J.*, vol. 2, no. 4, pp. 476–483, Dec 2008.
- [58] *MIL-HDBK-217F Military Handbook for Reliability Prediction of Electronic Equipment*, U. S. Department of Defense, Washington D.C., U.S.A., 1991.
- [59] *IRFP460 Power MOSFET Datasheet*, Vishay Siliconix, 2008, rev. A. [Online]. Available: <https://www.vishay.com/docs/91237/91237.pdf>
- [60] *IRFP250MPbF Power MOSFET Datasheet*, Infineon Technologies, 2020. [Online]. Available: https://www.infineon.com/dgdl/Infineon-IRFP250M-DataSheet-v01_01-EN.pdf?fileId=5546d462533600a4015356287bc71fda
- [61] S. E. De León-Aldaco, H. Calleja, F. Chan, and H. R. Jiménez-Grajales, "Effect of the mission profile on the reliability of a power converter aimed at photovoltaic applications—a case study," *IEEE Trans. Power Electron.*, vol. 28, no. 6, pp. 2998–3007, 2013.
- [62] H. Wang, M. Liserre, and F. Blaabjerg, "Toward reliable power electronics: Challenges, design tools, and opportunities," *IEEE Ind. Electron. Mag.*, vol. 7, no. 2, pp. 17–26, 2013.
- [63] A. Sangwongwanich, Y. Yang, D. Sera, and F. Blaabjerg, "Mission profile-oriented control for reliability and lifetime of photovoltaic inverters," *IEEE Trans. Ind. Appl.*, vol. 56, no. 1, pp. 601–610, 2020.
- [64] A. Sangwongwanich, H. Wang, and F. Blaabjerg, "Reduced-order thermal modeling for photovoltaic inverters considering mission profile dynamics," *IEEE Open Journal of Power Electronics*, vol. 1, pp. 407–419, 2020.



Yinxiao Zhu (S'19) was born in Guangdong, China, in 1995. He received the B.S. degree in micro-electronic science and engineering from the Tianjin University of Technology and Education, Tianjin, China, in 2017. He received the M.S. degree in sustainable energy technology from the University of Liverpool, Liverpool, U.K., in 2019, where he is currently working toward the Ph.D. degree.

His research interests include control for photovoltaic systems and power electronics.



Huiqing Wen (M'13–SM'18) received his B.S. and M.S. degrees in Electrical Engineering from Zhejiang University, Hangzhou, China, in 2002 and 2006, respectively. In 2009, he received his Ph.D. in Electrical Engineering from the Chinese Academy of Sciences, Beijing, China. From 2009 to 2010, he has been an electrical engineer working with the GE (China) Research and Development Center Company, Ltd., Shanghai, China. From 2010 to 2011, he was an engineer at the China Coal Research Institute, Beijing, China. From 2011 to 2012, he was

a postdoctoral fellow at the Masdar Institute of Science and Technology, Abu Dhabi, United Arab Emirates. In 2013, he joined the Electrical and Electronic Engineering Department of Xi'an Jiaotong-Liverpool University (XJTLU), Suzhou, China. Currently, he is an associate professor at the XJTLU. He has published more than 50 peer reviewed technical papers in leading journals. His research interests include renewable energy, electric vehicle, power electronics, microgrid, and power semiconductor devices.

He is the Associate Editor of IEEE ACCESS, International Journal of Photoenergy, and Journal of Power Electronics.



Guanying Chu (S'18) received the B.S. and M.S. degrees in electrical and electronic engineering from the University of Sheffield, Sheffield, U.K., in 2014 and 2015, respectively. He is currently working toward the Ph.D. degree in bidirectional dc/dc converter, advanced power electronics control with the University of Liverpool, Liverpool, U.K..

His current research interests include bidirectional dc–dc converter, digital control, and photovoltaic applications.



Xue Wang (S'20) was born in Hebei, China, in 1993. She received the B.S. degree in applied physics from Hebei Agricultural University, Baoding, China in 2015. In 2020, she received the master degree in sustainable energy from Xi'an Jiaotong-Liverpool University, Suzhou, China. She is currently working toward the Ph.D. degree at the University of Liverpool, U.K..

Her current research interests include power electronic, dc-dc converter, and photovoltaic applications.



Qilin Peng received his B.S. degree from Harbin Institute of Technology, Weihai, China in 2020. He is currently an Assistant Researcher in Xi'an Jiaotong-Liverpool University.

His current research interests include power electronics and photovoltaic system.



Yihua Hu (M'13–SM'15) received the B.S. degree in electrical engineering in 2003, and the Ph.D. degree in power electronics and drives in 2011, both at China University of Mining and Technology. Between 2011 and 2013, he was with the College of Electrical Engineering, Zhejiang University as a Postdoctoral Fellow. Between 2013 and 2015, he worked as a Research Associate at the power electronics and motor drive group, the University of Strathclyde. Between 2016 and 2019, he was a Lecturer at the Department of Electrical Engineering

and Electronics, University of Liverpool (UoL). Currently, he is a Reader at Electronics Engineering Department at The University of York (UoY). He has published over 100 papers in IEEE Transactions journals. His research interests include renewable generation, power electronics converters & control, electric vehicle, more electric ship/aircraft, smart energy system and non-destructive test technology.

He is the Associate Editor of IEEE Transactions on Industrial Electronics, IET Renewable Power Generation, IET Intelligent Transport Systems and Power Electronics and Drives. He is a fellow of Institution of Engineering and Technology (FIET). He was awarded Royal Society Industry Fellowship.



Lin Jiang (M'00) received the B.Sc. and M.Sc. degrees in electrical engineering from the Huazhong University of Science and Technology, Wuhan, China, and the Ph.D. degree in electrical engineering from the University of Liverpool, Liverpool, U.K., in 1992, 1996, and 2001, respectively. He was a Post-Doctoral Research Assistant with the University of Liverpool from 2001 to 2003 and a Post-Doctoral Research Associate with the Department of Automatic Control and Systems Engineering, University of Sheffield, Sheffield, U.K., from 2003 to 2005. He

was a Senior Lecturer with the University of Glamorgan, Wales, U.K., from 2005 to 2007, and joined the University of Liverpool in 2007. He is currently a Reader with the Department of Electrical Engineering and Electronics, University of Liverpool, U.K..

His current research interests include control and analysis of power system, smart grid, and renewable energy.